

# Discovery of materials with extreme work functions by high-throughput density functional theory and machine learning

Peter Schindler,<sup>1,2,\*</sup> Evan R. Antoniuk,<sup>3</sup> Gowoon Cheon,<sup>4</sup> Yanbing Zhu,<sup>1</sup> and Evan J. Reed<sup>1</sup>

<sup>1</sup>*Department of Materials Science and Engineering, Stanford University, Stanford, CA 94305, USA*

<sup>2</sup>*Faculty of Physics, University of Vienna, Vienna, Austria*

<sup>3</sup>*Department of Chemistry, Stanford University, Stanford, CA 94305, USA*

<sup>4</sup>*Department of Applied Physics, Stanford University, Stanford, CA 94305, USA*

The work function is the key surface property that determines how much energy is required for an electron to escape the surface of a material. This property is crucial for thermionic energy conversion, band alignment in heterostructures, and electron emission devices. Data-driven predictions of bulk material properties have been widely explored and work functions of elemental crystals have been studied thoroughly. However, the work functions of more complex compounds have not been investigated with a data-driven framework yet. Here, we present a high-throughput workflow using density functional theory (DFT) to calculate the work function of 29,270 surfaces (23,603 slab calculations) that we created from 2,492 bulk materials, including up to ternary compounds. Based on this database we develop a physics-based approach to featurize surfaces and use supervised machine learning to predict the work function. Our (random forest) model achieves a mean absolute test error of 0.19 eV, which is more than 4 times better than the baseline and comparable to the accuracy of DFT. This surrogate model enables rapid predictions of the work function ( $\sim 10^5$  faster than DFT) across a vast chemical space and facilitates the discovery of material surfaces with extreme work functions for energy conversion and electronic applications.

## Introduction

The work function is a fundamental surface parameter of a material that determines how much energy is required to extract an electron to a field-free region outside the surface; lower work functions facilitate electron emission at lower temperatures. Work functions play a key role in technologies that require precise control of contact barriers such as printed and organic electronics.[1–3] Materials with low work functions are crucial for electron emission devices (THz sources[4, 5] and fluorescent light bulbs[6]), electron sources for scientific instruments,[7, 8] and high-brightness photocathodes.[9] Especially, for thermionic energy converters (TECs)[10–12] discovery of thermally stable, ultra-low work function materials (less than 1.5 eV) would allow thermionic conversion of heat ( $> 1500$  °C) directly to electricity with efficiencies exceeding 30%. Materials with high work functions play a key role in engineering the electron tunneling barrier in electronics (for example in dynamic RAM applications[13] and for contacts in modern 2D-based transistors[14]) as well as selective contacts in solar cells[15].

The most commonly used materials for low work function applications that are chemically and thermally stable are compounds like lanthanum hexaboride[16, 17] and thoriated tungsten[18–21] with a work function around 2.5 eV. For thermionic converters, even lower work functions are required, which are achieved by sub-monolayer coatings of alkali metals (most commonly cesium) on metal surfaces. The resulting work functions are much lower than the work function of either metal or coating individually. This effect is due to the partial transfer of electron charge from the adsorbate to the substrate and the result-

ing formation of surface dipoles that lower the vacuum energy level near the surface.[22] Coatings using both cesium and oxygen are well known to achieve  $\sim 1$  eV work functions in photocathode applications, for instance on III-V semiconductors or silver.[23, 24] Diamondoids[25] and phosphorous-doped diamond thin films have shown similarly low work functions.[26] More recently, a work function of 1.01 eV has been achieved by electrostatically gating cesium/oxygen covered graphene,[27] which resulted in enhanced TEC efficiency.[28] The lowest experimentally measured work function has been obtained by inducing a surface photovoltage on Cs/O<sub>2</sub> coated Gallium Arsenide.[29] The lowest theoretically predicted steady-state value to date is 0.7–0.8 eV for potassium adsorbed on monolayers of MoTe<sub>2</sub> or WTe<sub>2</sub>. [30]

In recent years, data-driven approaches based on high-throughput *ab-initio* calculations has emerged as a new paradigm to facilitate the search through vast chemical spaces for new materials with tuned properties or novel behavior. Due to the continued increase in computing power and improvements of theoretical methods, the accuracy of predicted material properties has reached a reliability comparable to experiments while greatly surpassing them in terms of speed and cost. The rapid increase in available computational data structured in open source material databases such as Materials Project (MP),[31] AFLOW,[32] and NOMAD[33] has opened an avenue towards material discovery using data-mining and statistically driven machine learning approaches. However, most big material databases largely lack to report surface properties like the work function as each bulk material typically has dozens of distinct low-index crystalline surfaces and terminations. Each unique surface must be generated and calculated separately increasing the complexity and computational effort required. In the MP database this

\* peter.schindler@univie.ac.at

has only been done for  $\sim 100$  polymorphs of elemental crystals.[34] Based on several thousand newly predicted 2D materials[35] there are two other databases[36, 37] that report *ab-initio* work functions. It is straight-forward to calculate the work function for 2D materials as they have only one surface that is relevant. The JARVIS-DFT and the C2DB databases have work functions calculated for about 600 and 3000 surfaces, respectively.

Some statistical analyses have been carried out in literature showing that the electronegativity is linearly correlated with the work function both for elemental crystals and binary compounds.[34, 38] Additionally, for elemental crystals an inverse correlation with the atomic radius is pointed out. The work function of elemental crystals ranges between 2 and 6 eV (for Cesium and Selenium, respectively). The statistical analyses of about 30 binary compounds shows that a correlation between the electronegativity of the atom with the lower electronegativity is the strongest (better than arithmetic or geometric mean of the individual electronegativities). Density functional theory (DFT) has been a well-established approach (using a slab configuration) to calculate the work function, similar to the more simplistic Jellium model.[39] Also a phenomenological model has been developed that is able to estimate the work function fairly accurately for metals and alkaline-metal coated surfaces.[40] This phenomenological equation is a function of the atomic radius and the number of atomic sites per unit cell area. However, it relies on a single parameter (loosely related to the number of electrons that an atom can donate to the surface) that is not clearly defined for more complex surfaces and takes on nonphysical values in the case of alkaline coatings. Very recently, Hashimoto et al.[41] attempted to screen for low and high work function materials using a Bayesian optimization approach. However, they assume the work function to be approximated solely as a bulk property neglecting any surface contributions during screening. For the highest and lowest “bulk work function” material candidates the actual surface contributions haven then been included which rendered most of their top candidate materials to exhibit average work functions between 3 and 6 eV. Unsurprisingly, among their top candidate materials, they have found that the (110) surface of elemental Cesium has a low work function of 2.0 eV and that the (111) surface of  $\text{KEuO}_2$  has a relatively high work function of 8.4 eV. The approximated bulk work function of some of the screened work function candidates differs as much as 7 eV from the actual work function when including the surface contributions. This clearly shows that, while for simple structures (such as elemental metals) the work function can theoretically be predicted from bulk properties alone,[42] it is important to consider surface contributions to qualitatively and quantitatively predict the work function of a material. The surface termination, atom adsorption (most commonly Oxygen and Hydrogen), contamination, and reconstructions can affect the surface dipole and hence the effective work function. In this paper, we use high-throughput density functional

theory to calculate the work function of 29,270 surfaces created from 2,492 bulk crystal structures (up to ternary compounds). The created database gives insight into work function trends observed across a large chemical space. Based on the database we develop a machine learning model with a low mean absolute test-error of 0.19 eV which is more than 4 times lower than the baseline (i.e., predicting every surface to have the database-average work function) and about 3 times better than state-of-the-art benchmarking machine learning models (automatminer and Coulomb matrix). The database and machine learning model enable us to identify several promising material surfaces with extremely low ( $< 1.5$  eV) and extremely high ( $> 8$  eV) work functions.

## Methods

**High-throughput work function calculations.** The workflow of the work function database’s creation is illustrated in Figure 1. A total of 2,492 crystal structures were queried from the Materials Project (on 7/9/2020) using the REST framework.[31, 43] Up to ternary materials with 5 or less atoms in the unit cell were considered that have an energy above hull of less than 0.2 eV/atom and are tagged as an experimental structure (i.e., there exists at least one ICSD entry that reports the corresponding material as experimentally synthesized). Materials with an element present that is radioactive, a noble gas or from the actinoid group were excluded. Further, materials that have experimental tags that indicate high pressure or low temperature conditions, as well as low-dimensional materials were excluded as well. The frequency with which each chemical species appears in the database (bulk compounds) is plotted as a heat-map on the periodic table in Figure S1.

From this set of materials, surfaces up to a Miller index of 1 were generated using Pymatgen’s surface module.[34, 44, 45] Each surface orientation generally has more than one unique surface termination. The Pymatgen surface module has the option to generate slabs with different terminations determined by possible shifts in the  $c$ -direction. However, this may result in surfaces that are actually not unique because two terminations with distinct  $c$ -positions might actually be equivalent taking into account a shift in the  $a$  or  $b$  directions (or a rotation in the  $a$ - $b$  plane). To ensure that we generate all possible *unique* terminations we developed an algorithm based on the local environment of surface atoms, as summarized in the dashed block in Figure 1. First, a list of nearest neighbors (considering only atoms above the reference atom, i.e. with a larger  $c$ -component, up to a cutoff radius of 7 Å) with their distances and chemical elements are compiled for each atom in the slab. Atoms with identical nearest neighbor lists are grouped together into local environment groups (LEGs). In the second step, for each atomic layer (i.e., atoms with the same  $c$ -component considering a tolerance of 0.05 Å) the LEG of all atoms in the layer is grouped into a list (one list per layer of atoms). Thirdly, to determine the number

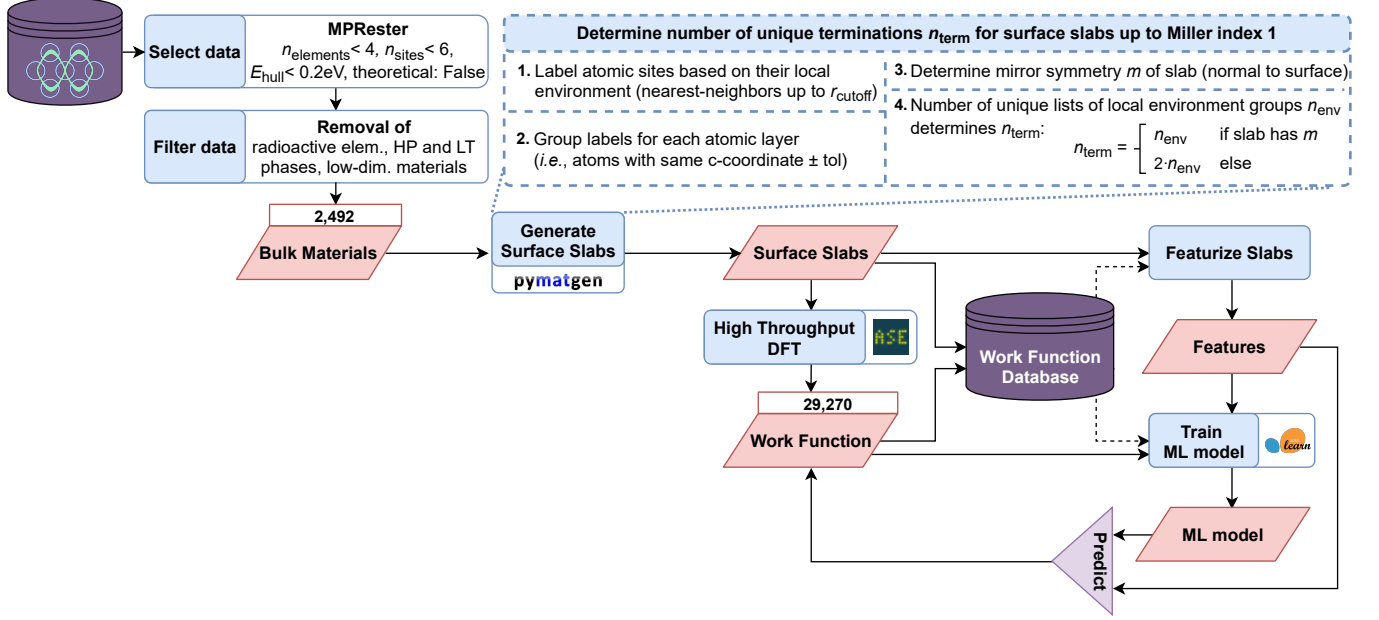


**Figure 1** | workflow of the creation of the work function database and surrogate machine learning model. The illustration includes the steps for material selection, high-throughput DFT calculations, surface slab creation, and supervised machine learning predictions. The dashed block details the procedure of determining the unique terminations of all surfaces up to a Miller index of 1.

of unique terminations  $n_{\text{term}}$ , we check whether the slab exhibits a mirror plane parallel to the surface. Finally, the number of unique lists of LEGs  $n_{\text{env}}$  determines the number of unique terminations  $n_{\text{term}}$  as follows:  $n_{\text{term}} = n_{\text{env}}$  if the slab has a mirror symmetry determined in step 3, or  $n_{\text{term}} = 2n_{\text{env}}$  else. This is due to the fact that the local environments are determined in the positive  $c$ -direction (only above the reference atom). Hence, a termination A on one side of the slab with termination B underneath might not be equivalent to the A termination on the other side if there is no mirror symmetry (e.g., the terminations in the following case may not be equivalent: **ABABABA**, where  $AB \neq BA$ ). Hence, to minimize redundancies we check whether the slab exhibits mirror symmetry in the  $c$ -direction (in the previous example, the slab has 2 unique terminations in case of a mirror symmetry and has 4 unique terminations otherwise). According to  $n_{\text{term}}$  we subtract the appropriate number of atomic layers to generate slabs with all unique terminations. Further, we minimize the number of slabs required for the DFT calculations by having two distinct terminations on either side of the slab, whenever possible. The initial slab thickness is minimized while still ensuring that after all necessary subtractions the final slab is at least 10 Å thick. Following this procedure, we create 24,334 slabs of which 23,603 converged during self-consistent field calculations with a total computational time of around 105,000 core-hours. The converged slabs returned a total of 29,270 unique surfaces and their work functions (where 8,131 surfaces had been removed due to being identified as duplicates during featurization).

**Density Functional Theory.** The work function is calculated by gradient-corrected DFT using the PBE exchange-correlation functional.[46] Self-consistent, periodic, total energy calculations are performed using Quantum Espresso (v.6.4.1).[47] Ultrasoft Vanderbilt pseudopotentials[48] are used to describe core electron interactions and the Kohn-Sham one-electron valence states are expanded in a plane wave basis set with a kinetic energy cutoff of 400 eV. The electron density is expanded up to ten times the energy of the plane wave energy cutoff. An extra 30 unoccupied bands are added for holding valence electrons to improve convergence. All slabs generated by the high-throughput procedure described above have a minimum thickness of 10 Å and 15 Å of vacuum between periodic slab repetitions in the  $c$ -direction to preclude interactions between periodic images. Brillouin zone sampling is performed under a grid spacing of less than  $0.05 \text{ \AA}^{-1}$  with finite-temperature Gaussian smearing ( $\sigma = 0.1 \text{ eV}$ ). A dipole correction is applied in the  $c$ -direction. The work function is determined by the difference of the electrostatic energy in the vacuum region and the Fermi energy. The PBE exchange-correlation functional has previously been shown to give reliable work functions for elemental crystals in agreement with experimental values with errors below 0.3 eV, which is comparable to the experimental precision.[49] The DFT calculation inputs for Quantum Espresso are automatically generated with the atomic simulation environment (ASE)[50] Python package and submitted into a high performance computing queuing system (SLURM) using job arrays. To estimate the convergence accuracy of the DFT-calculated work functions we reran  $\sim 1\%$  of the database

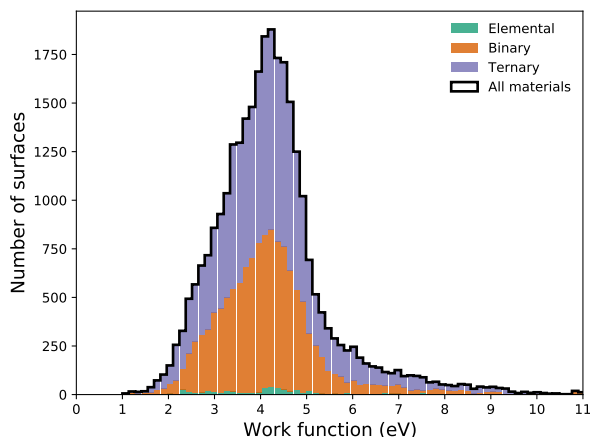


**Figure 2** | Distribution of the DFT-calculated work function database plotted as a stacked histogram. Outline corresponds to overall distribution under which the stacked, colored bars signify the number of surfaces based on elemental, binary, and ternary compounds. The average of the distribution is 4.22 eV with a standard deviation of 1.25 eV.

	Average	St.Dev.	Minimum	Maximum
Elemental	4.27	1.36	2.0	8.4
Binary	4.17	1.19	1.0	11.2
Ternary	4.26	1.29	0.9	11.4
All	4.22	1.25	0.9	11.4

**Table 1** | Detailed work function distribution metrics for elemental, binary, and ternary compounds. All values in eV.

(randomly selected) with stricter convergence parameters (energy cutoff of 700 eV and Brillouin zone sampling with a grid spacing of  $\leq 0.02 \text{ \AA}^{-1}$ ). The resulting mean absolute error and root-mean square error determined are 0.03 and 0.04 eV, respectively.

**Supervised Learning.** The dataset is randomly split into training and test sets (90/10 split) and the hyperparameters are optimized implementing 10-fold cross-validation on the training set. Multivariate linear regression, random forest, and neural network models are set up with the scikit-learn package in Python. The custom featurization procedure is laid out in the results and discussion section. As mentioned above, this featurization procedure resulted in 8,131 surfaces with duplicate features which were removed from the dataset before training. For benchmarking purposes we used the automatminer testing suite[51] and a conventional Coulomb matrix (topmost 10 surface atoms as input,  $\ell_2$ -sorted, with a random forest model).[52] For automatminer we use the “express” setting and for comparison we used the bulk unit cell and the topmost 5 atomic layers of the surface slabs as inputs.

## Results and Discussion

**Analysis of Work Function Database.** First, we analyze the work function database created by high-throughput DFT (29,128 surfaces based on 2,492 bulk crystals) in

terms of its distribution and trends in the studied chemical space. The work function distribution of the database is plotted in Figure 2 and shows a near-Gaussian distribution with an extended tail towards higher work functions. The average of the entire distribution is at 4.22 eV with a standard deviation of 1.25 eV, ranging from a minimum to a maximum work function of 0.9 to 11.4 eV, respectively. The stacked bar-chart signifies which proportion of the surfaces within each bin stems from an elemental, binary, or ternary compound. Their distribution metrics are given in Table 1.

The observation that the distribution in work functions is near-Gaussian could indicate that the chemical space we chose was diverse enough to evenly sample work functions across possible values. The extended tail at the high work function end appears to be an artifact coming from ionically unrelaxed surfaces where a small, electronegative atom (e.g. oxygen, hydrogen) is cleaved at a large, unphysical distance. This might also be the case for the low work function tail but appears to be less pronounced. This artifact can be mitigated by ionically relaxing the surface slabs and we expect this would result in an overall slightly narrower distribution. Interestingly, the work function distributions of binary and ternary compounds (and to a certain extent also the elemental crystals) have similar averages, standard deviations, and ranges.

Trends in the work function based on which chemical species are present at the surface are shown in Figure 3. The fraction of surfaces with a low work function ( $< 3$  eV, i.e., roughly one standard deviation below average) is especially high for surfaces with alkali, alkaline, or lanthanides present in the topmost atomic layer. Conversely, the fraction of surfaces with a high work function ( $> 6$  eV, i.e., roughly one standard deviation above average) is especially high for surfaces with halogens or oxygen present in the topmost atomic layer, as well as carbon, nitrogen, sulfur, and selenium (cf. Figure 3a). The total number of surfaces (rather than fractions) are shown in Figure S2.

The average work function is plotted as a heat-map based on the chemical species present in the topmost two atomic layers. The trends observed in Figure 3a are also seen in the average work function trend in Figure 3b. However, additionally one can observe trends based on combinations of chemical species in the topmost and second atomic layers. For example, the work function average is larger for surfaces where oxygen is present in the first layer and hydrogen in the second layer. In contrast, the work function average is lower for surfaces with halogens present in either first or second layer and nitrogen in the respective other layer. Further trends are plotted in Figures S3 (barchart of average work function as a function of the chemical species present at the topmost layer) and S4 (heat-maps showing percentage and total number of low and high work function surfaces as a function of chemical species present in the top two layers).

The trends described generally agree with the chemical intuition that surfaces terminated with electropositive

atoms from the alkali, alkaline, and lanthanide groups give a low work function, whereas electronegative atoms from the non-metal groups cause increased work functions. However, it is interesting to note that while  $\sim 40\%$  of surfaces that have an alkali/alkaline metal present in the topmost atomic layer have work function below 3 eV, still  $\sim 60\%$  have work functions above 3 eV, contrary to chemical intuition.

**Machine Learning Model for Work Function Predictions.** The large database created by high-throughput DFT calculations forms the basis for a surrogate machine learning model that enables the prediction of the work function at a fraction of the computational cost. As a first step, we assess common models from the materials science machine learning community as a benchmark. For that, we employ the automatminer testing suite,[51] and a conventional Coulomb matrix (topmost 10 surface atoms as input,  $\ell_2$ -sorted, trained with a random forest model).[52] For automatminer we use the “express” setting and compare using the bulk unit cell and the topmost 5 atomic layers of the surface slabs as inputs. As a baseline model we predict the work function to be the average work function regardless of the surface. The automatminer model performs only marginally better than the baseline model when bulk structures are used as an input. When the surface slabs are used as inputs the performance increases and is comparable to the performance of the Coulomb matrix. The mean absolute errors (MAEs) are shown for the training and test sets in Figure 4a. The baseline MAE is 0.90 eV and the DFT accuracy is indicated in the green-shaded area between 0.03 and 0.3 eV, corresponding to the convergence error (see Methods) and the error between PBE-calculated and experimental work functions,[49] respectively.

It is not surprising that the model performance is poor when the bulk structure is used as an input as the database contains multiple surfaces of different work functions for any given bulk structure. While the performance of the benchmarking models improves when the surface slab is used as the input instead, the MAEs are still large. This is likely due to the fact, that the models cannot distinguish between top and bottom of the input slab (which in general are not symmetric) and the database consists all unique terminations. In general, if one termination (located at the top surface) is labeled with the calculated work function, the same termination exists in another input structure at the bottom surface (whereas the calculated work function always refers to the top surface).

We developed a custom featurization of the surface slabs by considering physically motivated features of the topmost three surface layers (atoms grouped into the layers within a tolerance in  $c$ -direction of 0.3 Å, see effect of tolerance value on model performance in Figure S5). The considered atomic features are electronegativity  $\chi$ , inverse atomic radius  $1/r$ , first ionization energy  $E_{\text{ion}}$ , and Mendelev number  $n_{\text{mend}}$ . Given that each layer may contain more than one atom-type, we consider the minimum,

maximum, and average of each of these atomic features. This gives a total of 36 elemental features for the topmost 3 layers. Additionally, we add structural features: The packing fraction for each layer (number of atoms per unit cell area)  $A_{\text{pack}}^{-1}$  and the distances between atomic layers 1 and 2,  $d_{1-2}$ , and between layers 1 and 3,  $d_{1-3}$ . Out of this total 41 features the most significant features are selected with recursive feature elimination (RFE) using a random forest model, as plotted in Figure 4b. The best 6 features largely account for the model performance:  $\langle \chi_1 \rangle$ ,  $\min(\chi_1)$ ,  $\min(1/r_1)$ ,  $\min(E_{\text{ion},1})$ ,  $d_{1-2}$ , and  $A_{\text{pack},1}^{-1}$ . For the final model we use the best 15 features, which are the 6 features mentioned above and  $\langle \chi_2 \rangle$ ,  $\langle 1/r_1 \rangle$ ,  $\max(E_{\text{ion},1})$ ,  $\langle E_{\text{ion},2} \rangle$ ,  $\langle n_{\text{mend},1} \rangle$ ,  $\min(n_{\text{mend},1})$ ,  $d_{1-3}$ ,  $A_{\text{pack},2}^{-1}$ , and  $A_{\text{pack},3}^{-1}$ . It is worth noting that the majority of features we selected were physics-motivated or based on correlations observed in literature. The work function has been shown to linearly correlate with electronegativity for elemental crystals and binary compounds,[34, 38], and inversely correlate with the atomic radius. Another work has proposed a phenomenological equation for the work function that depends on the atomic radius and the number of atomic sites per unit cell area at the surface.[40] We chose the ionization energy as a feature based on physical intuition that low ionization energies lead to easy electron extraction. Lastly, the Mendelev number has been shown to be a descriptive feature for many material property predictions.[53, 54] Interestingly, the most predictive features (top 6) are features from the topmost layer (including the layer distance  $d_{1-2}$ ). This is in agreement with the fact that clear trends are observed considering only the topmost surface (cf. Figure 3a). Also, we note that we tried adding further elemental features without a clear physics-based motivation (e.g. polarizability) as well as further modes (e.g. geometric mean, range, variance) – however, this did not improve the model performance. Using this featurization approach (with 15 features) outperforms all benchmarking models (automatminer, in comparison, uses 200 features) even when a linear regression model is chosen, as seen in Figure 4a. When a non-linear learning model is used (neural network or random forest model) the MAEs are significantly reduced. Our best model using random forests has a test-MAE of 0.19 eV, comparable to the accuracy of work function calculations employing DFT. This test performance is about 3 times better than the best benchmarking model and more than 4 times better than the baseline. Figure 5 shows the predicted work function for both the training and test sets in comparison to the DFT calculated values. The kernel-density estimate distributions for both training and test sets are plotted for predicted and actual work functions showing that the predicted distribution is qualitatively faithful to the actual one. Notably, for the neural network and random forest models there is still a gap between training and test MAEs despite thorough hyperparameter tuning. This gap may be closed by adding more data in the future.

The prediction of the work function using this model

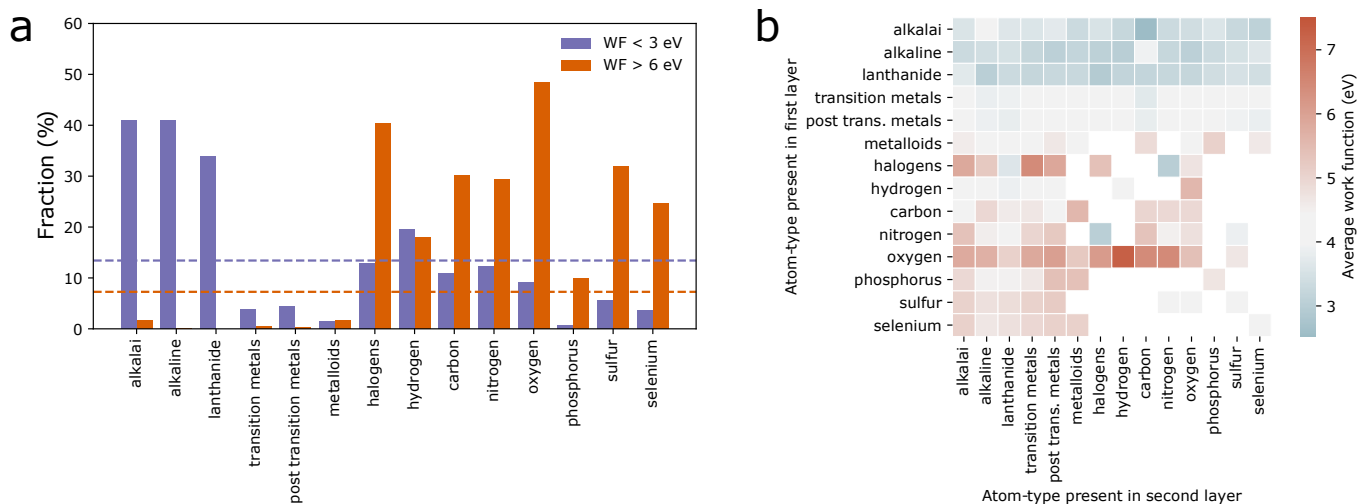


**Figure 3** | Work function trends observed in the database. **a** Fraction of material surfaces that have a work function below 3 eV (purple) and above 6 eV (orange) is shown depending on which type of chemical species is present at the topmost surface. The dashed lines indicate the average fraction across the entire database. **b** Heat-map of the average work function plotted as a function of chemical species present at the topmost layer (vertical axis) and second atomic layer (horizontal axis). The color bar displays work functions below and above average as blue and red, respectively. Categories with a population of less than 10 surfaces have been left blank.

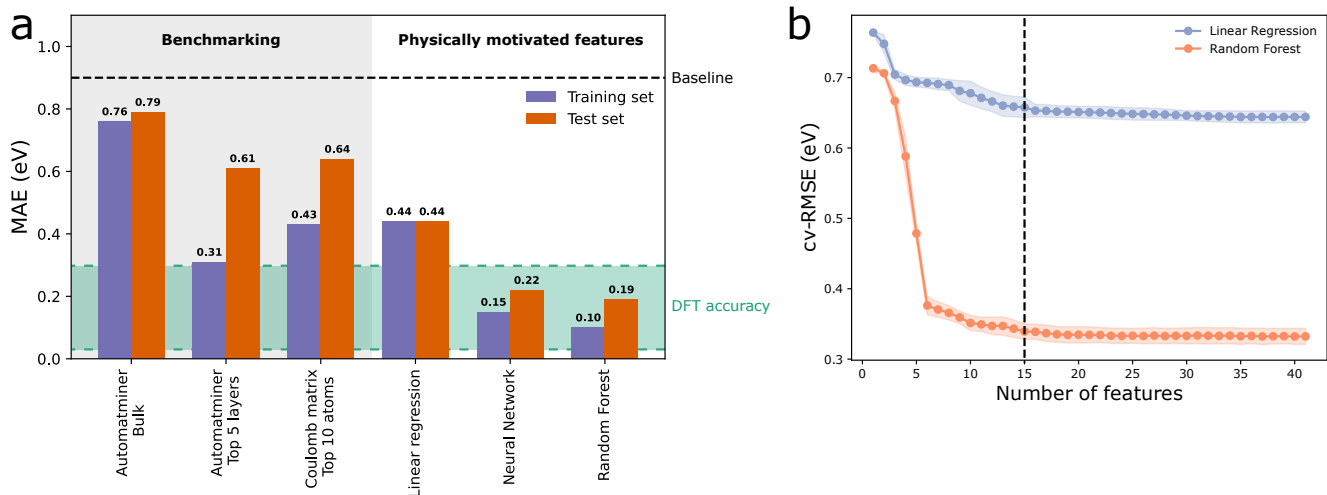


**Figure 4** | Comparison of machine learning model performances. **a** Mean absolute errors (MAEs) of training and test sets are given for this paper’s machine learning models: Linear regression, neural network, and random forest implementing 15 physically motivated features. The benchmarking models (automatminer with bulk unit cells and with surface slab of topmost 5 atomic layers as inputs, and a Coulomb matrix of the topmost 10 surface atoms,  $\ell_2$ -sorted, with a random forest model) are shown in comparison. The baseline model (always guessing the average work function) and the DFT accuracy are indicated by a dashed line and green-shaded area, respectively. **b** 5-fold cross-validated root mean square error (RMSE) as a function of number of input features is shown. Features were selected by recursive feature elimination for linear regression and random forest model. The top 15 most predictive features were selected for the final models.

is roughly  $10^5$  faster than DFT while having a MAE comparable to the accuracy of DFT. The database and the machine learning models are available at [github.com/peterschindler/WorkFunctionDatabase](https://github.com/peterschindler/WorkFunctionDatabase) enabling other researchers (including experimentalist) to use this model for work function predictions or to improve on our model performance.

For future work, this model may be extended to include surface relaxations during the high-throughput DFT cal-

culations which could enable the prediction of the work function of a relaxed surface solely based on features derived from the unrelaxed structure. Another improvement would be to consider the surface energy to determine which surface termination (and orientation) is the most stable one, similar to work by Palizhati et al.[55] Combining these two models could render an effective model for predicting the experimentally most relevant surface work function for each bulk compound.

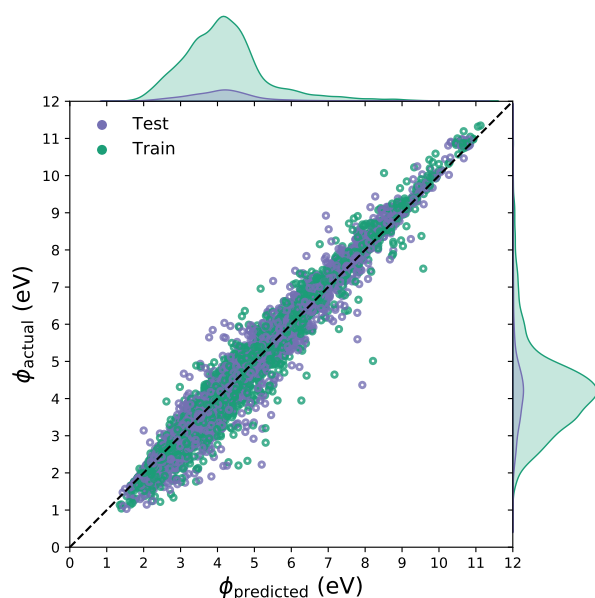


**Figure 5** | Predicted work functions vs. DFT calculated work functions. The kernel-density estimate distributions for both training and test sets are plotted for predicted and actual work function distributions at the top and right, respectively.

## Conclusions

In summary, we demonstrate a workflow to create a work function database from high-throughput DFT calculations that enables us to establish a surrogate machine learning model for rapid work function predictions. Our model has a MAE comparable to the accuracy of DFT while being  $\sim 10^5$  times faster. Using this approach facilitates the probing of a vast chemical space for novel material surfaces with exceptionally low or high work functions.

## Author Information

**Corresponding author.** \*E-mail: peter.schindler@univie.ac.at

## Acknowledgement

P.S. gratefully acknowledges financial support from the Austrian Science Fund (FWF) under contract J3980-N27. Further, he would like to extend gratitude to Prof. Jan Torgersen for proving access to computing resources.

## References

- [1] Y. Zhou, C. Fuentes-Hernandez, J. Shim, J. Meyer, A. J. Gior-dano, H. Li, P. Winget, T. Papadopoulos, H. Cheun, J. Kim, M. Fenoll, A. Dindar, W. Haske, E. Najafabadi, T. M. Khan, H. Sojoudi, S. Barlow, S. Graham, J.-L. Brédas, S. R. Marder, A. Kahn, and B. Kippelen, *Science* **336**, 327 LP (2012).
- [2] L. Lindell, A. Burquel, F. L. E. Jakobsson, V. Lemaure, M. Berggren, R. Lazzaroni, J. Cornil, W. R. Salaneck, and X. Crispin, *Chemistry of Materials* **18**, 4246 (2006).
- [3] A. L. Dadlani, P. Schindler, M. Logar, S. P. Walch, and F. B. Prinz, *The Journal of Physical Chemistry C*, 24827 (2014).
- [4] R. Snapp, J.P., Lee, J.-H., Provine, J., Bargatin, I., Maboudian, R., Lee, T.H., Howe, in *Solid-State Sensors, Actuators and Microsystems Workshop, Hilton Head* (2012) p. 336.
- [5] R. K. Barik, A. Bera, R. S. Raju, A. K. Tanwar, I. K. Baek, S. H. Min, O. J. Kwon, M. A. Sattarov, K. W. Lee, and G.-S. Park, *Applied Surface Science* **276**, 817 (2013).
- [6] S. Watanabe, T. Watanabe, K. Ito, N. Miyakawa, S. Ito, H. Hosono, and S. Mikoshiba, *Science and Technology of Advanced Materials* **12**, 34410 (2011).
- [7] J. Voss, A. Vojvodic, S. H. Chou, R. T. Howe, and F. Abild-Pedersen, *Physical Review Applied* **2**, 1 (2014).
- [8] M. Trenary, *Science and Technology of Advanced Materials* **13**, 23002 (2012).
- [9] E. R. Antoniuk, Y. Yue, Y. Zhou, P. Schindler, W. A. Schroeder, B. Dunham, P. Pianetta, T. Vecchione, and E. J. Reed, *Physical Review B* **101**, 235447 (2020).
- [10] J.-H. Lee, I. Bargatin, B. K. Vancil, T. O. Gwinn, R. Maboudian, N. A. Melosh, and R. T. Howe, *Journal of micromechanical systems* **23**, 1182 (2014).
- [11] J. H. Lee, I. Bargatin, N. A. Melosh, and R. T. Howe, *Applied Physics Letters* **100** (2012), 10.1063/1.4707379.
- [12] J. W. Schwede, T. Sarmiento, V. K. Narasimhan, S. J. Rosenthal, D. C. Riley, F. Schmitt, I. Bargatin, K. Sahasrabud-dhe, R. T. Howe, J. S. Harris, N. A. Melosh, and Z.-X. Shen, *Nature communications* **4**, 1576 (2013).
- [13] Y. Kim, P. Schindler, A. L. Dadlani, S. Acharya, J. Provine, J. An, and F. B. Prinz, *Acta Materialia* **117**, 153 (2016).
- [14] S. Chuang, C. Battaglia, A. Azcatl, S. McDonnell, J. S. Kang, X. Yin, M. Tosun, R. Kapadia, H. Fang, R. M. Wallace, and A. Javey, *Nano Letters* **14**, 1337 (2014).
- [15] P. Schulz, J. O. Tiepelt, J. A. Christians, I. Levine, E. Edri, E. M. Sanehira, G. Hodes, D. Cahen, and A. Kahn, *ACS Applied Materials & Interfaces* **8**, 31491 (2016).
- [16] J. Pelletier and C. Pomot, *Applied Physics Letters* **34**, 249 (1979).
- [17] P. L. Kanitkar, C. V. Dharmadhikari, D. S. Joag, and V. N. Shukla, *Journal of Physics D: Applied Physics* **9**, L165 (1976).
- [18] W. B. Nottingham, *Phys. Rev.* **49**, 78 (1936).
- [19] A. King, *Phys. Rev.* **53**, 570 (1938).
- [20] J. A. Sillero, D. Ortega, E. Muñoz-Serrano, and E. Casado, *Journal of Physics D: Applied Physics* **43**, 185204 (2010).
- [21] A. Bergner, M. Westermeier, C. Ruhrmann, P. Awakowicz, and J. Mentel, *Journal of Physics D: Applied Physics* **44**, 505203 (2011).
- [22] S. H. Chou, J. Voss, I. Bargatin, A. Vojvodic, R. T. Howe, and F. Abild-pedersen, *Journal of Physics: Condensed Matter* **24**, 445007 (2012).
- [23] J. J. Uebbing and L. W. James, *Journal of Applied Physics* **41**, 4505 (1970).
- [24] L. W. James, G. A. Antypas, J. Edgecumbe, R. L. Moon, and R. L. Bell, *Journal of Applied Physics* **42**, 4976 (1971).
- [25] K. T. Narasimha, C. Ge, J. D. Fabbri, W. Clay, B. A. Tkachenko, A. A. Fokin, P. R. Schreiner, J. E. Dahl, R. M. K. Carlson, Z. X. Shen, and N. A. Melosh, *Nature Nanotechnology* **11**, 267 (2015).

- [26] F. A. M. Koeck, R. J. Nemanich, A. Lazea, and K. Haenen, *Diamond and Related Materials* **18**, 789 (2009).
- [27] H. Yuan, S. Chang, I. Bargatin, N. C. Wang, D. C. Riley, H. Wang, J. W. Schwede, J. Provine, E. Pop, Z.-X. Shen, P. A. Pianetta, N. A. Melosh, and R. T. Howe, *Nano Letters* **15**, 6475 (2015).
- [28] H. Yuan, D. C. Riley, Z.-X. Shen, P. A. Pianetta, N. A. Melosh, and R. T. Howe, *Nano Energy* **32**, 67 (2017).
- [29] P. Schindler, D. C. Riley, I. Bargatin, K. Sahasrabudde, J. W. Schwede, S. Sun, P. Pianetta, Z. X. Shen, R. T. Howe, and N. A. Melosh, *ACS Energy Letters* **4**, 2436 (2019).
- [30] S. Kim, M. Y. Lee, S. Lee, and S.-h. Jhi, *Journal of Physics: Condensed Matter* **29**, 315702 (2017).
- [31] A. Jain, S. P. Ong, G. Hautier, W. Chen, W. D. Richards, S. Dacek, S. Cholia, D. Gunter, D. Skinner, G. Ceder, and K. A. Persson, *APL Materials* **1** (2013), 10.1063/1.4812323.
- [32] S. Curtarolo, W. Setyawan, S. Wang, J. Xue, K. Yang, R. H. Taylor, L. J. Nelson, G. L. Hart, S. Sanvito, M. Buongiorno-Nardelli, N. Mingo, and O. Levy, *Computational Materials Science* **58**, 227 (2012).
- [33] C. Draxl and M. Scheffler, *MRS Bulletin* **43**, 676 (2018), arXiv:1805.05039.
- [34] R. Tran, Z. Xu, B. Radhakrishnan, D. Winston, W. Sun, K. A. Persson, and S. P. Ong, *Scientific Data* **3**, 160080 (2016).
- [35] G. Cheon, K. A. N. Duerloo, A. D. Sendek, C. Porter, Y. Chen, and E. J. Reed, *Nano Letters* **17**, 1915 (2017).
- [36] S. Hastrup, M. Strange, M. Pandey, T. Deilmann, P. S. Schmidt, N. F. Hinsche, M. N. Gjerding, D. Torelli, P. M. Larsen, A. C. Riis-Jensen, J. Gath, K. W. Jacobsen, J. J. Mortensen, T. Olsen, and K. S. Thygesen, *2D Materials* **5** (2018), 10.1088/2053-1583/aacfc1.
- [37] K. Choudhary, I. Kalish, R. Beams, and F. Tavazza, *Scientific Reports* **7**, 1 (2017).
- [38] S. Yamamoto, K. Susa, and U. Kawabe, *The Journal of Chemical Physics* **4076**, 4076 (1974).
- [39] N. D. Lang and W. Kohn, *Physical Review B* **3**, 1215 (1971).
- [40] I. Brodie, S. H. Chou, and H. Yuan, *Surface Science* **625**, 112 (2014).
- [41] W. Hashimoto, Y. Tsuji, and K. Yoshizawa, *The Journal of Physical Chemistry C* **124**, 9958 (2020).
- [42] S. Halas and T. Durakiewicz, *Vacuum* **85**, 486 (2010).
- [43] S. P. Ong, S. Cholia, A. Jain, M. Brafman, D. Gunter, G. Ceder, and K. A. Persson, *Computational Materials Science* **97**, 209 (2015).
- [44] S. P. Ong, W. D. Richards, A. Jain, G. Hautier, M. Kocher, S. Cholia, D. Gunter, V. L. Chevrier, K. A. Persson, and G. Ceder, *Computational Materials Science* **68**, 314 (2013).
- [45] R. Tran, X. G. Li, J. H. Montoya, D. Winston, K. A. Persson, and S. P. Ong, *Surface Science* **687**, 48 (2019).
- [46] J. P. Perdew, K. Burke, and M. Ernzerhof, *Phys. Rev. Lett.* **77**, 3865 (1996).
- [47] P. Giannozzi and Others, *Journal of Physics: Condensed Matter* **21**, 395502 (2009).
- [48] K. F. Garrity, J. W. Bennett, K. M. Rabe, and D. Vanderbilt, *Computational Materials Science* **81**, 446 (2014).
- [49] S. De Waele, K. Lejaeghere, M. Sluydts, and S. Cottenier, *Physical Review B* **235418**, 1 (2016).
- [50] A. H. Larsen, J. J. Mortensen, J. Blomqvist, I. E. Castelli, R. Christensen, M. Dulak, J. Friis, M. N. Groves, B. Hammer, C. Hargus, E. D. Hermes, P. C. Jennings, P. B. Jensen, J. Kermode, J. R. Kitchin, E. L. Kolsbjerg, J. Kubal, K. Kaasbjerg, S. Lysgaard, J. B. Maronsson, T. Maxson, T. Olsen, L. Pastewka, A. Peterson, C. Rostgaard, J. Schiøtz, O. Schütt, M. Strange, K. S. Thygesen, T. Vegge, L. Vilhelmsen, M. Walter, Z. Zeng, and K. W. Jacobsen, *Journal of Physics: Condensed Matter* **29**, 273002 (2017).
- [51] A. Dunn, Q. Wang, A. Ganose, D. Dopp, and A. Jain, *npj Computational Materials* **6**, 1 (2020), arXiv:2005.00707.
- [52] L. Himanen, M. O. Jäger, E. V. Morooka, F. Federici Canova, Y. S. Ranawat, D. Z. Gao, P. Rinke, and A. S. Foster, *Computer Physics Communications* **247**, 106949 (2020), arXiv:1904.08875.
- [53] G. Cheon, E. D. Cubuk, E. R. Antoniuk, L. Blumberg, J. E. Goldberger, and E. J. Reed, *Journal of Physical Chemistry Letters* **9**, 6967 (2018).
- [54] P. Villars, K. Cenxual, J. Daams, Y. Chen, and S. Iwata, *Journal of Alloys and Compounds* **367**, 167 (2004).
- [55] A. Palizhati, W. Zhong, K. Tran, S. Back, and Z. W. Ulissi, *Journal of Chemical Information and Modeling* **59**, 4742 (2019).